Nano Energy 125 (2024) 109542

Contents lists available at ScienceDirect

Nano Energy

journal homepage: www.elsevier.com/locate/nanoen

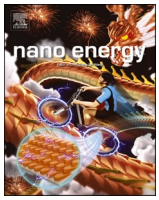

Small molecule donor third component incorporating thieno[3,2-*b*] thiophene unit enables 19.18% efficiency ternary organic solar cells with improved operational stability

Jing Li [a,1], Chenyang Zhang [a,b,1], Xiaokang Sun [b], Han Wang [c], Hanlin Hu [b,*], Kai Wang [a,*], Mingjia Xiao [d,*]

[a] Institute of Flexible Electronics (IFE), Northwestern Polytechnical University (NPU), Xi'an 710072, China
[b] Hoffman Institute of Advanced Materials, Shenzhen Polytechnic University, 7098 Liuxian Boulevard, Shenzhen 518055, China
[c] School of Management, Xián Polytechnic University, Xián, China
[d] The Quzhou Affiliated Hospital of Wenzhou Medical University, Quzhou People's Hospital, China

ARTICLE INFO

Keywords:
Ternary organic solar cells
Small molecular donor
Thieno[3, 2-*b*]thiophene (TT) side chain

ABSTRACT

The rational design of the third component to enhance the efficiency and stability of organic solar cell (OSC) is a critical and challenge. Herein, a thieno[3,2-*b*]thiophene (TT) substituted wide-bandgap small molecule donor BTTC, was designed, synthesized and incorporated into the state-of-the-art PM6:L8-BO binary to construct ternary OSC. The rigid side chain and planar molecule skeleton enables strong crystallinity and complementary absorption with binary system. The introduction of BTTC enhanced the molecular packing, fibril-like film and preferred vertical phase separation, yielding balanced and higher charge transport, more efficient exciton dissociation and suppressed charge recombination. Besides, lower energy loss was attained and thus leading to higher open-circuit voltage (V_{OC}). Consequently, the introduction of BTTC achieved the highest efficiency of 18.8% along with extended operational stability. Furthermore, replacing L8-BO to BTP-eC9 further boosted the ternary PCE to 19.18%, standing one of the best charge management in ternary OSC. This work presents efficient rigid side chain substitution strategy to construct the third component of small molecule donor for high performance ternary OSCs with comprehensively improved photovoltaic parameters. This strategy broadens the selection of guest materials toward realizing the actual commercial application of OSCs.

1. Introduction

Organic solar cells (OSCs) have advanced by leaps and bounds as an emerging next-generation photovoltaic technology due to the excellent qualities of solution processing, flexibility, and semitransparency [1–5]. Thanks to the development of novel Y series acceptors, the power conversion efficiency (PCE) of OSCs has exceeded 19%, approaching the threshold of industrial application [6–10]. However, the development of OSC is still limited by large energy loss and strong charge recombination [11–13]. Apart from the new donor/acceptor materials, morphology regulation is crucial for further improving the performance of OSCs. Multiple strategies have been reported for adjusting the morphology of OSCs, including solvent/thermal annealing, ternary strategy and solvent/solid additives, which have been widely adopted by the state-of-the-art OSCs [14–16]. Among these strategies, the solvent/solid strategy is proved as simple and effective method to manipulate the morphology. However, the high boiling points of commonly used solvent additives such as 1-chloronaphthalene (CN) and 1,8-diiodooctane (DIO) made them difficult to volatilize, the residue can induce morphology degradation and reduce reproducibility and stability [17]. Recently, solid additives have emerged as promising alternative to solvent additives [18]. Zhang group proposed the commonly building block benzo[1,2-*b*:4,5-*b*']dithiophene (BDT) as a solid additive. The crystallinity and charge transfer were enhanced and a PCE of 17.91% was achieved for the BDT-treated PM6:Y6 OSCs [19]. While, it is also worth noting that solvent/solid additive strategy is mainly used to manipulate the morphology. For the ternary method, in addition to the morphology regulation, the complementary absorption between the third component

* Corresponding authors.
E-mail addresses: hanlinhu@szpu.edu.cn (H. Hu), kaiwang@nwpu.edu.cn (K. Wang), qyctmb@wmu.edu.cn (M. Xiao).
[1] J. Li and C. Zhang contributed equally to this work.

https://doi.org/10.1016/j.nanoen.2024.109542
Received 15 February 2024; Received in revised form 21 March 2024; Accepted 22 March 2024
Available online 24 March 2024

and binary is also achieved to boost the photon energy harvesting. Moreover, the appropriate third component might play a positive role in facilitating charge dynamic processes, such as providing additional charge transport channels, helping exciton separation at interfaces, accelerating charge extraction. Therefore, the ternary can achieve the concurrent improvement of all the three key parameters in OSCs [20–23]. Besides, the required higher temperature to fully remove the solvent/solid additives might reduce open-circuit voltage (V_{OC}) and restrict the potential of PCE [24–26].

Generally, the third component material can be classified to polymers and small molecules. Compared to polymers, small molecules feature advantage of definite molecular structure, easier purification, and less batch-to-batch issue. Up to now, a large proportion of TOSCs were constructed with two acceptors owing to their small miscibility difference, easily tuned energy levels and high crystallinity. Table S1 (Support information, SI) summarized most TOSCs literatures with >18% PCEs constructed by two Y-series acceptors [27–33]. Y-series acceptors as the third component adopt molecular strategy including alkyl chains difference and asymmetry to regulate molecular crystallinity. For example, Chen group reported the asymmetric acceptor BTP-S9 with stronger crystallinity, and its introduction improved the crystallization and stacking of the PM6:L8-BO system. The PM6:BTP-S9:L8-BO ternary device yielded a PCE of 18.84% [34]. Yang group explored acceptors with symmetric and asymmetric hybrid cycloalkyl-alkyl chains to decrease the optical bandgap and deepen the energy level, the resultant PM6:Y-C10ch:L8-BO device achieved a higher PCE of 19.1% [35]. However, the synthesis of Y-series molecules is tedious and not friendly for commercial application. Compared to Y-series molecules, much less attention has been paid on small molecule donors (SMDs) third component, partially owing to the difficulty to fulfill the prerequisite of energy level alignment, complementary absorption and molecular crystallinity. Generally, the addition of appropriate SMDs third component could broaden the absorption and optimized the energy level. Besides, as most of SMDs possess strong crystallinity, it would be more desirable to optimize the morphology by introduction of SMDs [36–41].

Diverse strategies have been explored in the development of SMDs for TOSCs. In our previous studies, we adopted different end-groups of cyanooctyl ester and esterified rhodanine to fine-tune the electronics and crystalline properties of SMDs third component, the ternary device based on PM6:BT-ER:L8-BO achieved the PCE of 18.11% [42]. Furthermore, we developed two SMDs third component by isomerization engineering of chlorine substitution position, the result αBTCl achieved highest efficiency of 18.96% in PM6:L8-BO system and high thickness-tolerance property [43]. Except introducing halogen atoms to increase the crystallinity of SM donors [44], expanding the conjugated structure is also an effective strategy. For example, Ge group extended the conjugation of the molecular backbone and synthesized G19 with an extremely ordered edge-on orientation, resulting in a largely improved PCE of TOSC to 18.53% with D18-Cl:G19:Y6 system [45]. Hou *et al.* designed a wide-bandgap small molecule NRM-1 with rigid conjugate plane. NRM-1 can disperse into the acceptor phase in the PBDBT:IT-4 F-based OSC and reduce the E_{loss} of the TOSC [46]. Bao group incorporated DRTB-T-C4 molecule with high crystallinity into the host PM6:Y6 blend to construct TOSC, the ternary device PM6:DRTB-T-C4:Y6 reduced recombination loss and obtained a PCE of 17.13% [47]. These works demonstrated that the addition of high crystallinity SMDs to the binary system is conducive to the regulate morphology of blend film. On the other hand, most researchers believe that appropriate energy level to form a cascade energy level can promote efficient charge separation and transfer [48–50]. The requirement of deeper highest occupied molecular orbital (HOMO) level than polymer donor limits the choice of the third donor component. Therefore in the early stage, design strategies focus on the regulation of energy levels by chemical structure modification. However, with the emergence of high-performance binary system, improving the morphology and reducing the energy loss of the host device has become a more and more important consideration for the third component. Highly efficient TOSC devices are rarely reported based on a higher HOMO level than PM6 [51]. Therefore, it's worth exploring rational selection and new design strategy of the third component.

In this work, we designed and synthesized a wide bandgap SMD third component, BTTC, incorporating thieno[3,2-*b*]thiophene (TT) as the side chain of the BDT center core. The rigid TT unit was introduced into the BDT unit to enhance crystallinity [52–54]. The enhanced conjugation in the side chain direction is perpendicular to the molecular backbone, and thus will not significantly redshift the absorption and keep the complementary absorption with the binary system. The molecule possesses strong crystallinity and modest miscibility. The introduction into PM6:L8-BO binary device increased the crystallinity and induced preferred vertical phase separation, which leads to efficient charge extraction, balanced carrier mobility and suppressed charge recombination. Meanwhile, BTTC has a higher HOMO level than PM6 and a reduced energy loss was observed for the ternary device. Ultimately, the resultant ternary OSC achieved an excellent PCE of 18.8%, with a V_{OC} of 0.901 V, J_{SC} of 26.61 mA cm^{-2}, and FF of 78.42%. Meanwhile, the ternary device presented evidently extended operational stability. Furthermore, in order to verify the versatility of BTTC in high efficiency binary systems, ternary OSCs utilizing BTP-eC9 as the acceptor have also been studied. The PCE was further improved to 19.18% and the charge management (FF×J_{SC}) result is one of the highest value for ternary OSCs so far, higher than the recent solvent/solid additive treated devices (Table S2). This study provides a novel approach to fabricate high-performance ternary OSCs with all enhanced photovoltaic parameters by introducing a SMD featuring high HOMO level. This strategy could greatly widen the third component selection and further improve the efficiency and stability of ternary OSCs.

2. Results and discussion

2.1. Synthesis and properties

The chemical structures of PM6, L8-BO, BTTC are shown in Fig. 1**a**. In order to increase intermolecular π−π interactions, we choose thieno[3,2-*b*]thiophene (TT) unit as substitution of the central benzo[1,2-*b*:4,5-*b'*]dithiophene (BDT) core, and a long 2-hexyldecyl (HD) alkyl chain was introduced into the TT unit to guarantee sufficient solubility. Detailed synthetic route is illustrated in Scheme S1 in Supporting Information (SI). The target molecule was obtained *via* Stille coupling reaction with a yield of 59%. BTTC possesses good solubility and can be dissolved in common solvents such as chloroform, tetrahydrofuran. Molecular structure is characterized by the nuclear magnetic resonance (NMR) spectra (Fig. S1 and S2). Thermogravimetry analysis (TGA) measurement indicates superior thermal stability for BTTC with high T_d (decomposition temperature 5% weight loss) at temperature 372℃ (Fig. S3).

The optical properties of PM6, L8-BO and BTTC were investigated by UV–Vis absorption spectra (Fig. 1**b**). The film maximum absorption peak of BTTC (567 nm) exhibits an obvious redshift compared to its solution absorption (468 nm), indicating strong π−π interactions in the film state. The optical bandgap (E_g^{opt} =1240/λonset) of BTTC is calculated to be 1.86 eV according to the absorption edge (λonset) of 667 nm with absorption coefficient of BTTC film in Fig. S4. BTTC film possesses strong absorption in shorter wavelength range, implying complementary absorption with PM6:L8-BO system. The energy level was obtained by cyclic voltammetry measurement (Fig. S5 and S6). The HOMO level of BTTC was calculated to be −5.23 eV according to the equation E_{HOMO}= −E ($E_{onset,\ Ox}$+4.80−$E_{Fc/Fc+}$) (eV) [55], in which $E_{Fc/Fc+}$ is the redox potential of Fc/Fc$^+$ (0. 675 eV versus Ag/AgCl). The lowest unoccupied molecular orbital (LUMO) level is calculated to be −3.37 eV using the formula E_g^{opt} =E_{HOMO}−E_{LUMO}. The corresponding energy diagrams are presented in Fig. 1**c**. To better understand the effect of

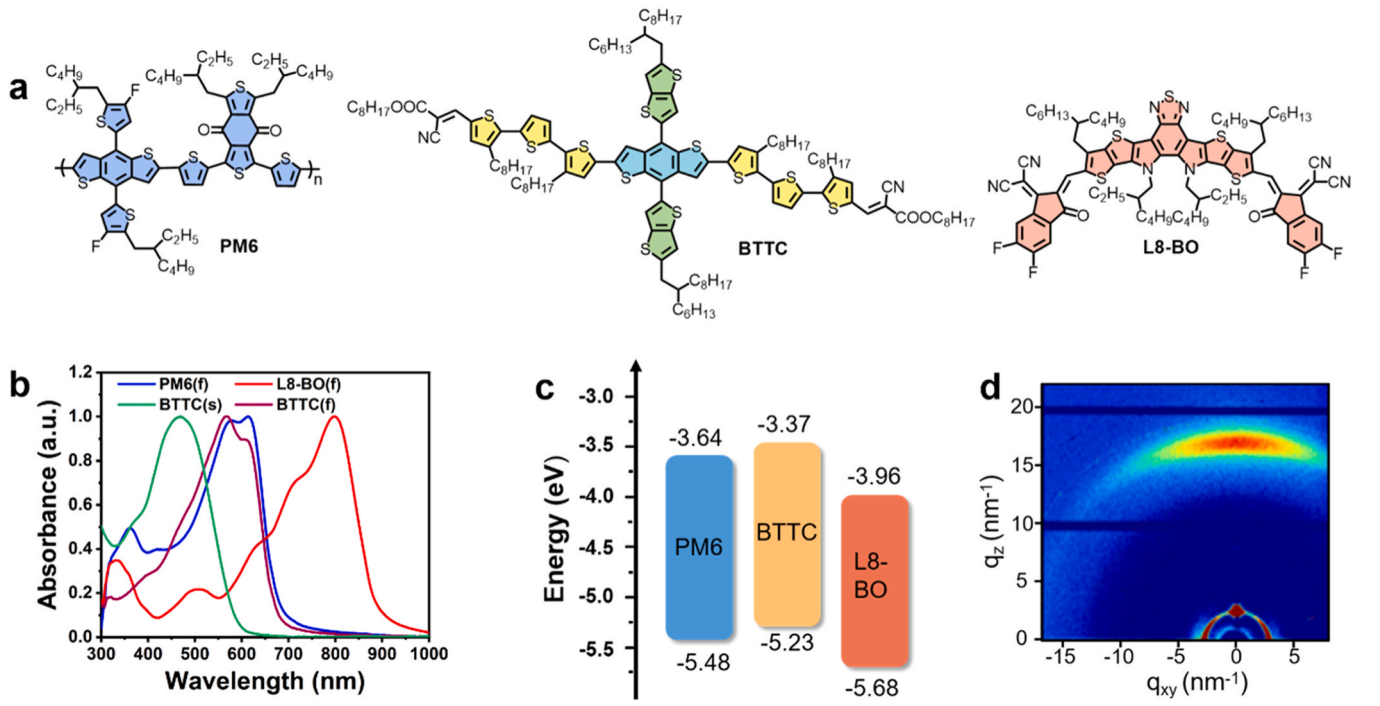

Fig. 1. Basic properties of the materials. (a) Chemical structures of PM6, BTTC, L8-BO. (b) Normalized thin film absorption spectra of PM6, L8-BO, BTTC and the solution absorption spectra of BTTC. (c) Energy levels diagram of PM6, L8-BO, BTTC. (d) 2D GIWAXS pattern of the neat BTTC film.

π-conjugation extension on the energy levels and molecular orbital distribution of BTTC, density functional theory (DFT) calculation was performed (Fig. S7). The long alkyl chains were simplified with the methyl groups to reduce the complexity of calculation. The E_{HOMO} and E_{LUMO} are calculated out −5.43/−3.19 eV, respectively. The HOMO was delocalized over the whole backbone and TT units, while the LUMO was mainly located in the end groups. The molecule displays excellent planarity, which is favorable for orderly molecular packing and the π-conjugation extension through molecular skeleton. The molecular packing properties of BTTC were investigated by grazing-incidence wide-angle X-ray scattering (GIWAXS) measurement (Fig. 1**d**), clear π–π stacking (010) scattering peak is observed in the out-of-plane (OOP) direction for BTTC film, suggesting BTTC has a preferential face-on orientation. Fig. S8 demonstrates BTTC film possesses strong diffraction signal locating at 0.29 Å^{-1} (d-spacing=21.66 Å) with calculated coherence lengths (CCL) of 144.92 Å, indicating the strong crystallinity.

2.2. Photovoltaic properties

To investigate the influence of BTTC on the ternary photovoltaic performance, we constructed OSCs with device architecture of ITO/poly (3,4-ethylenedioxythiophene):poly(styrene sulfonate) (PEDOT:PSS)/ active layer/N,N′-bis[3-[3- (dimethylamino)propylamino]propyl]perylene-3,4:9,10-bis (dicarbimide) (PDINN)/Ag, Fig. 2**a** presents the current density-voltage ($J-V$) curves of optimal devices under AM 1.5 G illumination at 100 mW cm^{-2}. Table 1 lists the detailed photovoltaic parameters of the binary and ternary devices. Detailed optimized device parameters are shown in the Table S3 and S4. The control PM6:L8-BO device delivered a V_{OC} of 0.881 V, J_{SC} of 26.26 mA cm^{-2}, and a FF of 78.04% with a PCE of 18.05%. Incorporating 0.05 wt% BTTC as the guest donor, the PM6:BTTC:L8-BO ternary device exhibited an obviously elevated V_{OC} of 0.901 V and J_{SC} of 26.61 mA cm^{-2}, and a higher FF of 78.42%, achieving a comparable PCE of 18.8%. Fig. S9 depicts the PCE distribution for the devices, statistics of 10 cells for each device, demonstrating PCE values reproducibility for each device with small deviations. We also have fabricated binary OSCs based on BTTC:L8-BO and BTTC:BTP-eC9, and obtained PCE of 3.28% and 5.35%, respectively (Fig. S10 and Table S5). The external quantum efficiency (EQE) spectra are illustrated in Fig. 2**b**. All the devices exhibited a broad and efficient photon-to-current conversion in the range of 300–1000 nm due to the spectral complementarity between PM6, BTTC and L8-BO. Compared with the binary device, the ternary device exhibits slightly higher response spectra in the short wavelength. The PM6:BTTC:L8-BO device holds the highest response (90%) at 570 nm, corresponding to the absorption peak of BTTC. The integrated current density based on the EQE curves (Table 1) agrees well with the J_{SC} values obtained from the $J-V$ measurements within 5% range. Stability is critical factors for the real applications. The devices stability of PM6:L8-BO and PM6:BTTC:L8-BO were examined with maximum power point (MPP) tracking under 1 sun illumination for 240 h (Fig. 2**c**) at N_2 atmosphere under room temperature. After MPP tracking for 24 h, the PCE of the PM6:L8-BO device decays by 20%. In contrast, the PM6:BTTC:L8-BO device shows a smaller decay with PCE decreased by only 4.8% after 240 hours, maintaining 80% of the original efficiency. The impact of BTTC on thermal stability of device was characterized. As shown in Fig. S11a, the PCE of PM6:L8-BO suffers from a severe drop to 80% of its initial value within 50 h at 60 ℃ in glove box. In contrast, the device based on PM6:BTTC:L8-BO shows notably enhanced thermal stability under the same operational condition, maintaining 94% of its initial PCE within 50 h. We further tracked the storage stability (Fig. S11b), BTTC-based ternary device kept 84% of the initial PCE after 240 h storing. While, the PCE of PM6:L8-BO kept only 31%. The significantly improved operational stability for ternary device might be originated from the suppressed light-induced trap defects. To investigate intermolecular dynamic processes between PM6 and BTTC, photoluminescence (PL) spectra were measured under 550 nm light excitation, as shown in Fig. S12. A strong PL emission peak is observed for neat BTTC film at 720 nm. The neat PM6 film exhibits relatively weak PL emission peak at 700 nm. Particularly, the PL emission intensity of PM6:BTTC blend film is monotonously decreased as PM6 content increasing, and BTTC emission peak in blend film is completely quenched at 720 nm, indicating the existence of energy transfer from BTTC to PM6.

Charge collection and recombination properties were characterized to understand the improved performance of ternary device. Firstly, we

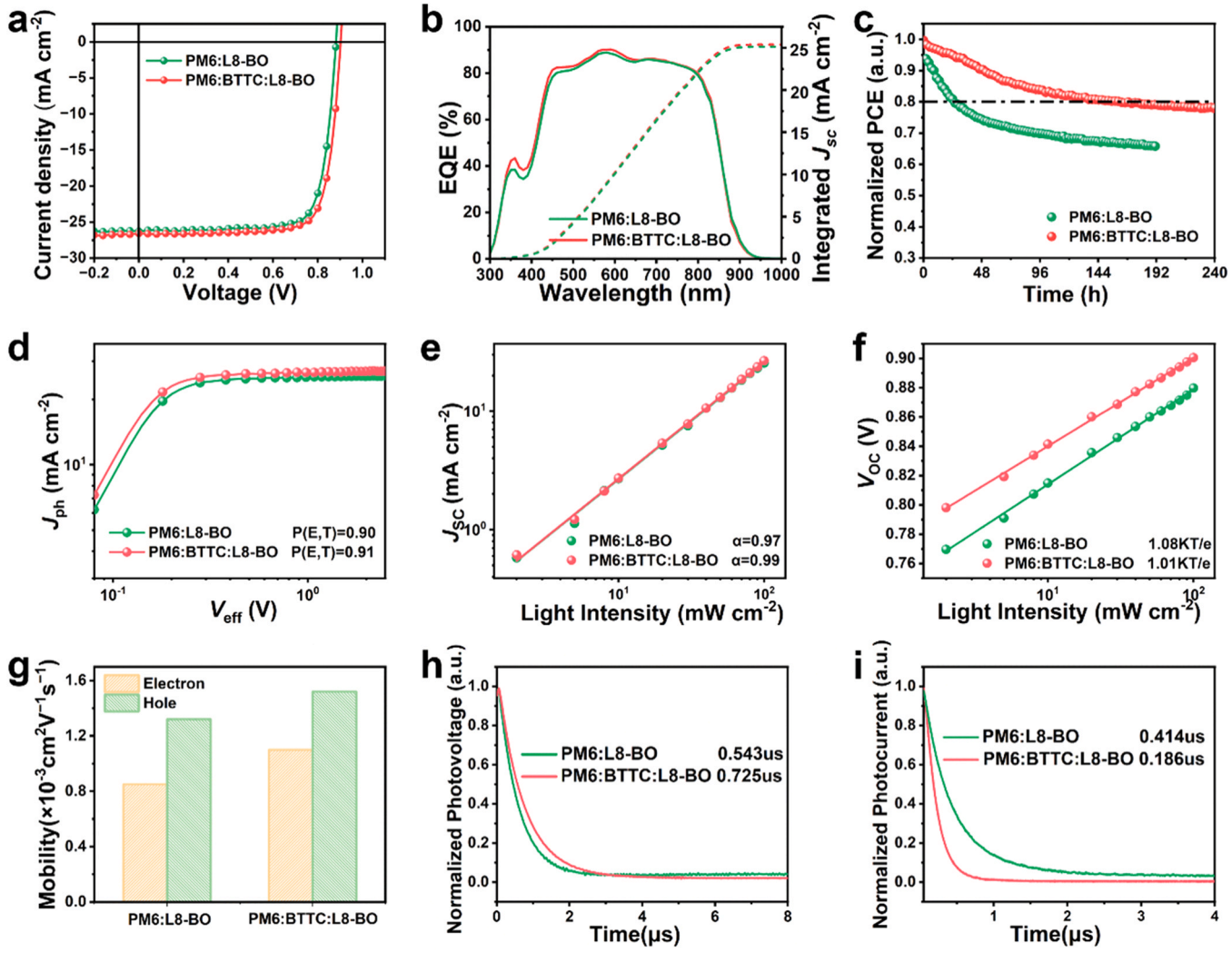

Fig. 2. Photovoltaic performance of OSCs. (a) $J-V$ curves for optimized OSCs. (b) EQE spectra and integrated current densities for optimized OSCs. (c) Light stability of binary and ternary devices with maximum power point (MPP) tracking under 1 sun illumination (d) $J_{ph}-V_{eff}$ curves. (e) J_{SC} and (f) V_{OC} versus light intensity. (g) The charge mobilities of the corresponding devices. (h) TPV and (i) TPC of PM6:L8-BO and PM6:BTTC:L8-BO devices.

Table 1
The detail photovoltaic parameter of binary and ternary devices [a]).

Active Layer	V_{OC} (V)	J_{SC} (mA/cm^2)	J_{SC}^{cal} (mA/cm^2)	FF (%)	PCE (%)
PM6:L8-BO	0.881 (0.880 ±0.0009)	26.26 (26.22 ±0.08)	25.1	78.04 (77.86 ±0.30)	18.05 (17.94 ±0.06)
PM6:BTTC:L8-BO	0.901 (0.902 ±0.0007)	26.61 (26.59 ±0.05)	25.4	78.42 (78.05 ±0.18)	18.80 (18.72 ±0.05)
PM6:BTP-eC9	0.850 (0.850 ±0.0005)	28.08 (27.94 ±0.12)	26.8	75.62 (75.65 ±0.36)	18.05 (17.97 ±0.05)
PM6:BTTC:BTP-eC9	0.853 (0.853 ±0.0009)	28.32 (28.29 ±0.09)	27.0	79.40 (78.98 ±0.29)	19.18 (19.06 ±0.06)

a)The average values within the parentheses were obtained with 10 devices.

measured the dependence of photocurrent density (J_{ph}) on effective voltage (V_{eff}). The J_{ph} is derived from the formula $J_{ph} = J_L - J_D$, where the J_L and J_D represent the light current density and the dark current density, respectively [56]. V_{eff} is the difference between V_0 (the voltage when $J_{ph} = 0$) and V (the applied bias). J_{sat} is the density of the saturated photocurrent when V_{eff} >2 V. The ratio of J_{ph}/J_{sat} can be evaluated the exciton dissociation probability ($P(E, T)$) [57]. As depicted in Fig. 2**d**, the $P(E, T)$ is 90% for optimized PM6:L8-BO and 91% for PM6:BTTC:L8-BO. The $P(E, T)$ values suggested that both the binary and ternary devices feature efficient charge collection process. Furthermore, the J_{SC} and V_{OC} values as a function of light intensity were measured to explore the charge recombination. The J_{SC} exhibits a dependence on light intensity (P_{light}) with the relationship $J_{SC} \propto P_{light}^{\alpha}$ (Fig. 2**e**), where α close to 1 implies that there almost no bimolecular recombination and free carriers are all collected [58]. The obtained values were 0.97 and 0.99 for the PM6:L8-BO binary and PM6:BTTC:L8-BO ternary device, respectively, indicating the slightly reduced bimolecular recombination in PM6:BTTC:L8-BO ternary device. The trap-assisted recombination was further evaluated by estimating the relationship of V_{OC} and P_{light} (Fig. 2**f**), where the slope close to 2 kT/q means that the device is dominated by trap-assisted recombination, while the slope close to 1 kT/q indicates that the device is dominated by bimolecular recombination (where T, k, and q are the Kelvin temperature, Boltzmann constant, and elementary charge, respectively) [59]. The slope of the PM6:L8-BO device (1.08 kT/q) is slightly higher than that of PM6:BTTC:L8-BO (1.01 kT/q), illustrating that the introduction of BTTC suppressed trap-assisted recombination for PM6:L8-BO. In short, the above results indicated that the introduction of BTTC could effectively

suppress the charge recombination and thus benefiting J_{SC} and FF.

To elucidate charge transport properties, the electron and hole mobilities (μ_e and μ_h) were measured by space-charge limited currents (SCLC) method. The curves of the electron-only and hole-only devices are depicted in Fig. S13, and the relevant parameters are listed in Table S6. The μ_h and μ_e values are 1.32×10^{-3} and 0.85×10^{-3} $cm^2V^{-1}s^{-1}$ for PM6:L8-BO device, respectively. In contrast, the ternary blend film (PM6:BTTC:L8-BO) exhibited improved charge transport properties with higher μ_h of 1.52×10^{-3} and μ_e of 1.1×10^{-3} $cm^2V^{-1}s^{-1}$, respectively (Fig. 2**g**). Moreover, the PM6:BTTC:L8-BO device exhibited a more balanced charge transfer ability ($\mu_h/\mu_e = 1.38$), suggesting that the charge transport process is more efficient and balanced in the ternary device. We also determined the mobilities (μ_h and μ_e) of neat BTTC film to investigate the influence of the TT substitution on carrier transport (Fig. S14). The μ_h and μ_e values are 1.99×10^{-4} and 1.58×10^{-7} $cm^2V^{-1}s^{-1}$ for neat BTTC film, respectively (Table S7). The improved charge transport by TT substitution agrees well with the device J_{SC} and FF values, which could benefit from the enhanced intermolecular interaction. We performed transient photovoltage (TPV) and transient photocurrent (TPC) measurements to further evaluate BTTC impact on charge extraction and charge carrier lifetime (Figs. 2**h** and 2**i**). The carrier lifetimes are 0.543, 0.725 μs for the PM6:L8-BO and PM6:BTTC:L8-BO devices, respectively, and the charge extraction times are calculated to be 0.414 and 0.186 μs for the PM6:L8-BO and PM6:BTTC:L8-BO, respectively. These results manifest that the ternary device has shorter charge carrier extraction time and longer charge carrier lifetime than PM6:L8-BO device. Apparently, the introduction of BTTC benefited the charge transport and extraction and suppressed the charge recombination of the device, thereby favored J_{SC} and FF of the ternary device.

2.3. Films morphology characteristics

To investigate the miscibility of BTTC with PM6 and L8-BO, the contact angles of the neat PM6, BTTC, and L8-BO films have been measured (Fig. 3**a**), and the detailed parameters are summarized in Table S8. The surface energy (γ) of PM6, BTTC and L8-BO films turned out to be 25.40, 19.54 and 29.49 mN m^{-1}, respectively (Fig. 3**b**), and the Flory-Huggins interaction parameters (χ) can be calculated via the equation $\chi = K(\sqrt{\gamma D} - \sqrt{\gamma A})^2$ to evaluate their miscibility [60]. The $\chi_{PM6:BTTC}$ and $\chi_{BTTC:L8-BO}$ parameters came out to be 0.38 K and 1.02 K (Fig. 3**b**), respectively. This indicates that BTTC is more inclined to form

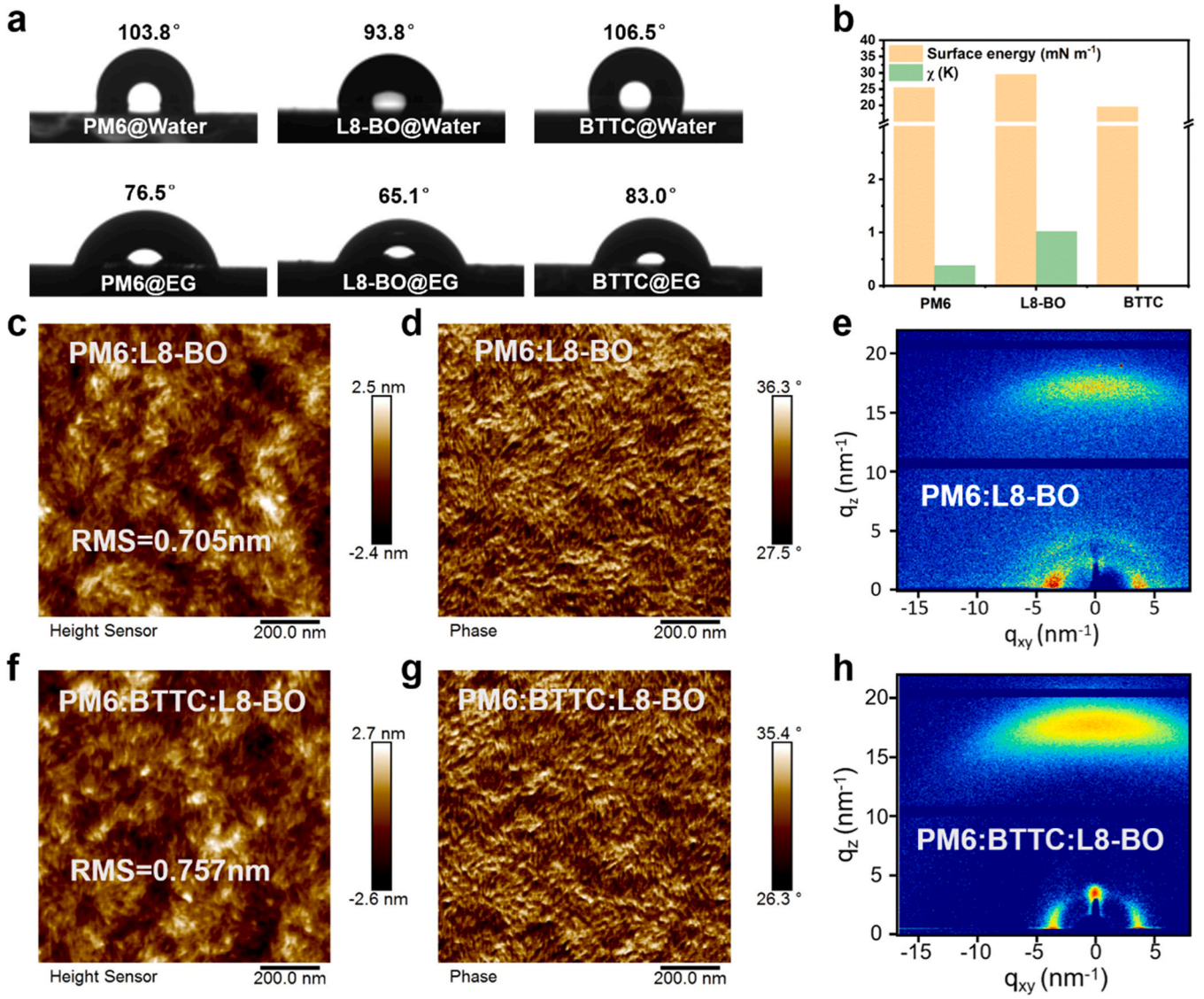

Fig. 3. Morphology characterizations of the blend films. (a) The contact angles of water and ethylene glycol (EG) drops on PM6, BTTC, and L8-BO blend films. (b) Surface tension values of the corresponding neat films and χ values between the PM6/L8-BO and BTTC. AFM height images of (c) PM6:L8-BO and (f) PM6:BTTC:L8-BO. AFM phase images of (d) PM6:L8-BO and (g) PM6:BTTC:L8-BO. GIWAXS images of blend film of (e) PM6:L8-BO; (h) PM6:BTTC:L8-BO.

non-separating phase with PM6. The incorporation of BTTC reduces the miscibility between PM6 and L8-BO, thereby promoting phase separation. The differential scanning calorimetry (DSC) of PM6:BTTC and L8-BO:BTTC blends at different weight ratios was performed (Fig. S15). The peak of BTTC appears at a ratio of 1:1 (wt/wt), and it could not be seen with ratio of 1:0.05 and 1:0.1 (PM6:BTTC). Whereas for L8-BO:BTTC blends, the BTTC peak could be clearly detected at ratio of 1:0.1 (L8-BO:BTTC), and the peak intensity increased with more amount of BTTC. Therefore, it was suggested BTTC was more incline to mix with PM6 than L8-BO. As presented in Fig. 3**c** and 3**f**, atomic force microscopy (AFM) was utilized to characterize the morphology properties. The root-mean squire roughness (RMS) of the PM6:BTTC:L8-BO ternary blend film (0.757 nm) slightly increased than the PM6:L8-BO binary film (0.705 nm), indicating that the PM6:BTTC:L8-BO blend film exhibited strengthened phase separation and widened nanofibrils due to the strong crystallinity of BTTC. Figs. 3**d** and 3**g** demonstrate nanoscale bicontinuous interpenetrating network structure of the ternary blend, which contributes to the suppressed charge recombination and a higher FF [61]. The fibril texture of PM6:L8-BO blend film is roughly defined with a smaller fibril diameter and more sparse fibril distribution. Adding BTTC into PM6:L8-BO improved the crystallinity of the blend film by forming a high-quality fibril network with increased fibril diameter and distribution (Fig. S16). To further explore morphology variations of the binary and ternary blend films, we performed GIWAXS measurement to investigate the molecular packing behavior. The binary and ternary blend films show preferred face-on orientation (Fig. 3**e** and 3**h**), and the GIWAXS 2D patterns are listed in Table S9 and Fig. S17. The PM6:L8-BO blend film shows face-on orientation at 1.76 $Å^{-1}$ (d=3.57 Å) in the out-of-plane (OOP) direction. Compared to the binary film, the ternary blend film depicts face-on orientation at 1.77 $Å^{-1}$ (d=3.55 Å) in the OOP direction, the diffraction peaks of PM6:BTTC:L8-BO blend film was significantly enhanced. Furthermore, the calculated crystal coherence length (CCL_{010}) value of PM6:BTTC:L8-BO blend film (20.19 Å) is higher than that PM6:L8-BO blend film (18.84 Å), implying that the introduction of BTTC not only strengthened phase separation, but also enhanced molecular ordering in ternary blend film. These results are consistent with the improved charge carrier mobility and FF in ternary device.

To investigate the vertical phase distribution of the binary and ternary blend films, film-depth-dependent light absorption spectroscopy (FLAS) was performed. Fig. 4**a** and 4**d** exhibit light absorption spectra of PM6:L8-BO and PM6:BTTC:L8-BO ternary blend films at different film depth (depth 0 and 95 nm represent the active layer/PDINN and active layer/PEDOT:PSS interface, respectively), the absorption peaks located at 628 nm are attributed to PM6, and the absorption around 800 nm predominantly originates from L8-BO. The L8-BO absorption of PM6:BTTC:L8-BO blend film exhibits apparent variation at different depths compared with binary device, which conducives vertical electron transport in the ternary blend film. Upon fitting the light absorption

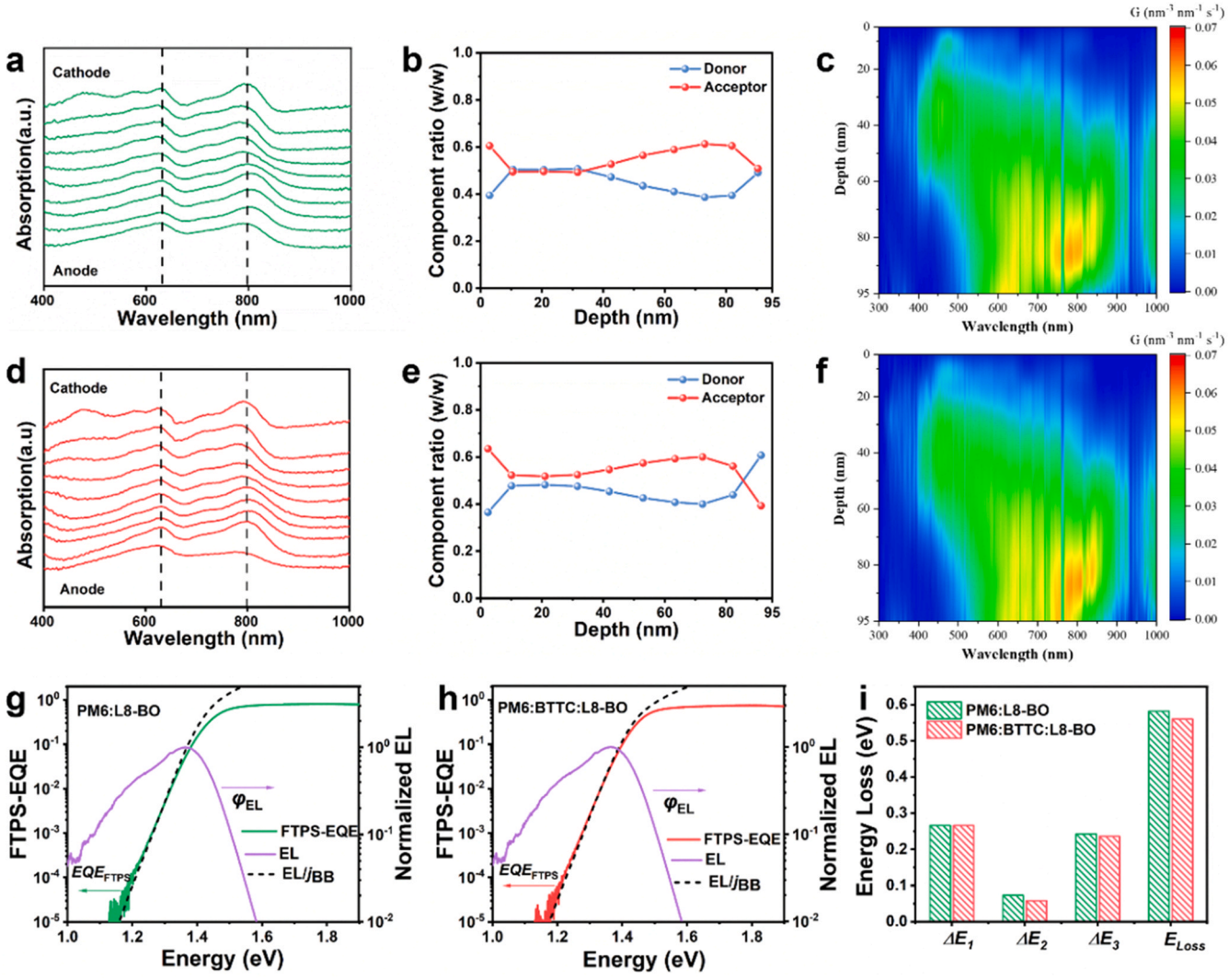

Fig. 4. Film-depth-dependent light absorption spectra and E_{loss} analysis. (a-c) binary and (d-f) BTTC-based ternary devices of Film-depth-dependent light absorption spectra. Normalized FTPS-*EQE*, EQE, and EL of the (g) PM6:L8-BO, (h) PM6:BTTC:L8-BO. (i) Comparison of ΔE_1, ΔE_2, and ΔE_3 values and E_{loss} histogram.

profiles of subfilms with the absorption spectra of PM6 and L8-BO films, the composition ratio of PM6 and L8-BO at different film depths can be extracted. As depicted in Fig. 4**b** and 4**e**, the PM6:BTTC:L8-BO blend film has a more well-defined double-layer interpenetrating structure, where both PM6 and L8-BO display a gradient distribution, with higher concentrations of PM6 near the anode and L8-BO near the cathode, respectively, contributing to the reduced bimolecular recombination and improve charge transfer [9,62]. Fig. 4**c** and 4**f** demonstrate the excitons are mainly produced at the bottom of the blend films. Compared with binary device, the number of exciton produced by the ternary blend film is higher near the anode region, supporting the favored gradient phase distribution vertically in the ternary device.

To understand the V_{OC} enhancement behavior, energy loss (E_{loss}) analysis of the binary and ternary devices were conducted. The detailed E_{loss} values are shown in Table S10 and Fig. 4**g**−**4i**. The E_g was measured from the EQE spectra of the blend films. As summarized in Table S10, the radiant energy loss (ΔE_1) represents the unavoidable radiative loss originating from absorption above the bandgap (E_g) [63] and there is no difference among binary and ternary devices. ΔE_2 is the loss of radiation recombination below the band gap, determined by the degree of energy disorder and recombination [64]. The ΔE_2 of ternary device (0.058 eV) is significantly lower than binary device (0.073 eV), suggesting minimized energy disorder in ternary device. ΔE_2 can be quantified by a parameter of the Urbach energy (E_U), and smaller E_U represents the lower energy disorder. By fitting FTPS-*EQE* with Urbach's rule [65], the E_U of the ternary device was 22.2 meV, lower than the binary device (24.2 meV) (Fig. S18). The reduced E_U was mainly attributed to the enhanced crystallinity of ternary blend film. ΔE_3 is measured according to the following equation [66]:

$\Delta E_3 = qV_{oc}^{non-rad} = -kTln(EQEEL)$Where EQE_{EL} is the electroluminescence quantum efficiency of the device. As shown in Table S10, the binary and ternary devices exhibit an EQE_{EL} of 8.1×10^{-3} and 1.07×10^{-2} (Fig. S19), corresponding ΔE_3 of 0.243 and 0.236 eV, respectively. Eventually, the ternary device achieves a lower E_{loss} of 0.56 eV than binary device (0.582 eV for PM6:L8-BO), which contributes to a higher V_{OC} of ternary device. Compared with PM6:L8-BO device, the reduction of E_{loss} for PM6:BTTC:L8-BO originates from both mitigation of ΔE_2 (from 0.073 to 0.058 eV) and ΔE_3 (from 0.243 to 0.236 eV), verifying that BTTC as the third component is a feasible way to reduce E_{loss} and improve the V_{OC}.

2.4. A universality of BTTC

Inspired by the favored effect of BTTC, we introduced BTTC into PM6:BTP-eC9 binary system to verify the universality. The control binary PM6:BTP-eC9 device achieved a PCE of 18.05%, with a V_{OC} of 0.85 V, a J_{SC} of 28.08 mA cm^{-2}, and a FF of 75.62% (Fig. 5**a**). By introducing BTTC (0.05 wt%) as the third component, PCE of the PM6:BTTC:BTP-eC9 ternary device remarkably enhanced to 19.18%, with impressively increased FF of 79.4% (Table 1 and Table S11). The narrow PCE distribution demonstrates the excellent reproducibility of the device (Fig. S7). The value of FF×J_{SC} can be utilized to represent charge management [67]. As presented in Fig. 5**c** and Table S1, the charge management value of PM6:BTTC:BTP-eC9 is one of the best result among those ternary OSCs, indicating BTTC as the third component can effectively optimize the morphology and suppress recombination to manufacture high-performance OSCs.

3. Conclusion

In summary, BTTC molecule with extended π-conjugated TT side chain pending on BDT block was designed, synthesized and incorporated into the binary PM6:L8-BO device to construct ternary device. BTTC exhibits strong crystallinity, modest miscibility and complementary absorption with PM6:L8-BO binary system. Thorough morphological studies unveil that the incorporation of BTTC enhanced the crystallinity and induced preferred vertical phase separation structure. This resulted in higher charge mobilities, suppressed carrier recombination and more efficient charge extraction and collection. Additionally, despite the HOMO level of BTTC does not favor the cascade alignment with the binary system, the reduced radiative and nonradiative recombination leads to decreased energy loss and thus benefits V_{OC} Consequently, relative to the PM6:L8-BO host blend, the ternary device achieved remarkable PCE of 18.8% with a synchronously improved V_{OC} of 0.901 V, J_{SC} of 26.61 mA cm^{-2}, and FF of 78.42%. Meanwhile, the PM6:BTTC:L8-BO blend film presented extended operational stability, which is beneficial for future practical applications. Impressively, the molecule BTTC was introduced into the PM6:BTP-eC9 system, the PM6:BTTC:BTP-eC9 exhibited an excellent PCE of 19.18% with superior charge management property. These results demonstrate that constructing cascade energy level alignment is not the prerequisite for the third component, and widen the design strategy for third component to achieve high-performance and stable ternary OSCs.

CRediT authorship contribution statement

Xiaokang Sun: Methodology. **Hanlin Hu:** Resources. **Jing Li:** Writing – original draft, Methodology, Formal analysis, Conceptualization. **Chenyang Zhang:** Validation, Methodology, Investigation. **Kai Wang:** Writing – review & editing, Supervision, Funding acquisition, Conceptualization. **Han Wang**: Calculation. **Mingjia Xiao**: review & editing.

Declaration of Competing Interest

The authors declare that they have no known competing financial interests or personal relationships that could have appeared to influence the work reported in this paper.

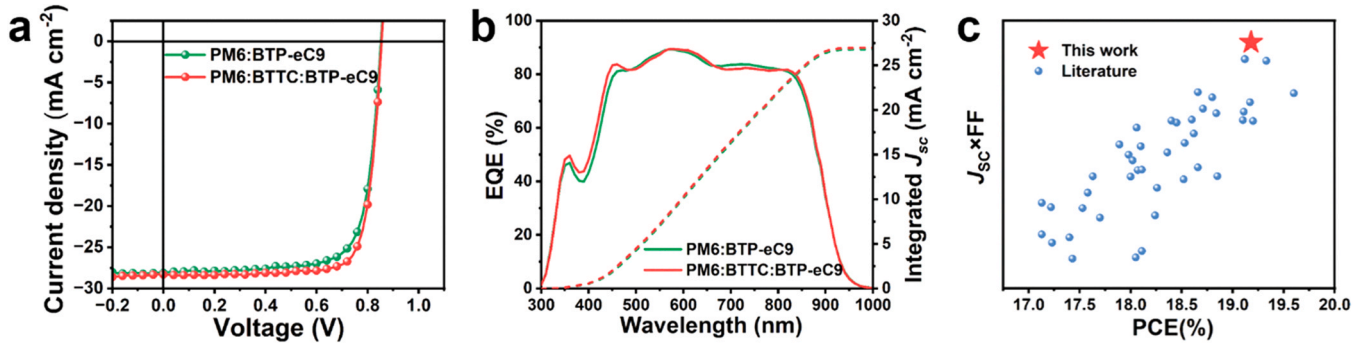

Fig. 5. Additional device information. (a) $J-V$ curves for optimized OSCs. (b) EQE spectra and integrated current densities for optimized OSCs. (c) Comparison of J_{SC}×FFs and PCEs of ternary device based on the champion solar cell in this work and results reported in the literature.

Data Availability

Data will be made available on request.

Acknowledgements

The authors thank the financial support from National Natural Science Foundation of China (62104197), and the Taishan Scholar Program of Shandong Province (No. tsqn201812050), and Innovation Foundation for Doctor Dissertation of Northwestern Polytechnical University (CX2023102).

Appendix Supporting Information

Supplementary data associated with this article can be found in the online version.

Appendix A. Supporting information

Supplementary data associated with this article can be found in the online version at doi:10.1016/j.nanoen.2024.109542.

References

[1] L. Zhu, M. Zhang, W. Zhong, S. Leng, G. Zhou, Y. Zou, X. Su, H. Ding, P. Gu, F. Liu, Y. Zhang, Progress and prospects of the morphology of non-fullerene acceptor based high-efficiency organic solar cells, Energy Environ. Sci. 14 (2021) 4341–4357.
[2] R. Sorrentino, E. Kozma, S. Luzzati, R. Po, Interlayers for non-fullerene based polymer solar cells: distinctive features and challenges, Energy Environ. Sci. 14 (2021) 180–223.
[3] J. Huang, H. Tang, C. Yan, G. Li, 1,1-Dicyanomethylene-3-indanone end-cap engineering for fused-ring electron acceptor-based high-performance organic photovoltaics, Cell Rep. Phys. Sci. 2 (2021) 100292.
[4] L. Lu, T. Zheng, Q. Wu, A.M. Schneider, D. Zhao, L. Yu, Recent advances in bulk heterojunction polymer solar cells, Chem. Rev. 115 (2015) 12666–12731.
[5] Z. Peng, Y. Zhang, X. Sun, W. Zhao, F. Bian, Y. Geng, L. Ye, C. Yang, Real-time probing and unraveling the morphology formation of blade-coated ternary nonfullerene organic photovoltaics with in situ X-ray scattering, Adv. Funct. Mater. 33 (2023) 2213248.
[6] X. Xu, W. Jing, H. Meng, Y. Guo, L. Yu, R. Li, Q. Peng, Sequential deposition of multicomponent bulk heterojunctions increases efficiency of organic solar cells, Adv. Mater. 35 (2023) 2208997.
[7] L. Zhan, S. Li, Y. Li, R. Sun, J. Min, Z. Bi, W. Ma, Z. Chen, G. Zhou, H. Zhu, M. Shi, L. Zuo, H. Chen, Desired open-circuit voltage increase enables efficiencies approaching 19% in symmetric-asymmetric molecule ternary organic photovoltaics, Joule 6 (2022) 662–675.
[8] Z. You, Y. Song, W. Liu, W. Wang, C. Zhu, Y. Duan, Y. Liu, Diazabicyclic electroactive ionenes for efficient and stable organic solar cells, Angew. Chem. Int. Ed. 62 (2023) 202302538.
[9] C. He, Y. Pan, G. Lu, B. Wu, X. Xia, C. Ma, Z. Chen, H. Zhu, X. Lu, W. Ma, L. Zuo, H. Chen, Versatile sequential casting processing for highly efficient and stable binary organic photovoltaics, Adv. Mater. 34 (2022) 2203379.
[10] L. Kong, Z. Zhang, N. Zhao, Z. Cai, J. Zhang, M. Luo, X. Wang, M. Chen, W. Zhang, L. Zhang, Z. Wei, J. Chen, In situ removable additive assisted organic solar cells achieving efficiency over 19% and fill factor exceeding 81%, Adv. Energy Mater. 13 (2023) 2300763.
[11] Z. Chen, W. Song, K. Yu, J. Ge, J. Zhang, L. Xie, R. Peng, Z. Ge, Small-molecular donor guest achieves rigid 18.5% and flexible 15.9% efficiency organic photovoltaic via fine-tuning microstructure morphology, Joule 5 (2021) 2395–2407.
[12] D. Zhou, W. You, H. Xu, Y. Tong, B. Hu, Y. Xie, L. Chen, Recent progress in ternary organic solar cells based on solution-processed non-fullerene acceptors, J. Mater. Chem. A 8 (2020) 23096–23122.
[13] L. Meng, Y. Zhang, X. Wan, C. Li, X. Zhang, Y. Wang, X. Ke, Z. Xiao, L. Ding, R. Xia, H. Yip, Y. Cao, Y. Chen, Organic and solution-processed tandem solar cells with 17.3% efficiency, Science 361 (2018) 1094–1098.
[14] D. Li, N. Deng, Y. Fu, C. Guo, B. Zhou, L. Wang, J. Zhou, D. Liu, W. Li, K. Wang, Y. Sun, T. Wang, Fibrillization of non-fullerene acceptors enables 19% efficiency pseudo-bulk heterojunction organic solar cells, Adv. Mater. 35 (2023) 2208211.
[15] R. Ma, X. Jiang, J. Fu, T. Zhu, C. Yan, K. Wu, P. Müller-Buschbaum, G. Li, Revealing the underlying solvent effect on film morphology in high-efficiency organic solar cells through combined ex situ and in situ observations, Energy Environ. Sci. 16 (2023) 2316–2326.
[16] D. Qiu, J. Zhang, K. Lu, Z. Wei, Halogenated thiophene substitutions on quinoxaline unit to achieve morphology optimization in efficient organic solar cells, Nano Res. 16 (2023) 11630–11637.
[17] B. Villers, K. O'Hara, D. Ostrowski, P. Biddle, S. Shaheen, M. Chabinyc, D. Olson, N. Kopidakis, Removal of residual diiodooctane improves photostability of high-performance organic solar cell polymers, Chem. Mater. 28 (2016) 876–884.
[18] J. Song, Y. Li, Y. Cai, R. Zhang, S. Wang, J. Xin, L. Han, D. Wei, W. Ma, F. Gao, Y. Sun, Solid additive engineering enables high-efficiency and ecofriendly all-polymer solar cells, Matter 5 (2022) 4047–4059.
[19] M. Dong, S. Chen, L. Hong, J. Jing, Y. Bai, Y. Liang, C. Zhu, T. Shi, W. Zhong, L. Ying, K. Zhang, F. Huang, 19.0% efficiency binary organic solar cells enabled by using a building block as solid additive, Nano Energy 119 (2024) 109097.
[20] R. Ma, C. Yan, J. Yu, T. Liu, H. Liu, Y. Li, J. Chen, Z. Luo, B. Tang, X. Lu, G. Li, H. Yan, High-efficiency ternary organic solar cells with a good figure-of-merit enabled by two low-cost donor polymers, ACS Energy Lett. 7 (2022) 2547–2556.
[21] F. Zhao, X. Zheng, S. Li, K. Yan, W. Fu, L. Zuo, H. Chen, Non-halogenated solvents processed efficient ITO-free flexible organic solar cells with upscaled area, Macromol. Rapid Commun. 43 (2022) 2200049.
[22] Y. Li, Y. Cai, Y. Xie, J. Song, H. Wu, Z. Tang, J. Zhang, F. Huang, Y. Sun, A facile strategy for third-component selection in non-fullerene acceptor-based ternary organic solar cells, Energy Environ. Sci. 14 (2021) 5009–5016.
[23] T. Ameri, P. Khoram, J. Min, C. Brabec, Organic ternary solar cells: a review, Adv. Mater. 25 (2013) 4245–4266.
[24] A. Classen, T. Heumueller, I. Wabra, J. Gerner, Y. He, L. Einsiedler, N. Li, G. Matt, A. Osvet, X. Du, A. Hirsch, C. Brabec, Revealing hidden UV instabilities in organic solar cells by correlating device and material stability, Adv. Energy Mater. 9 (2019) 1902124.
[25] H. Feng, Z. Liu, Y. Bao, B. Zhao, B. Wu, Z. Bi, W. Wu, W. Ma, C. Gao, An efficient enhancement in organic photovoltaics by introducing simple-structured benzo[1,2-b:4,5-b']dithiophene-based large-bandgap small molecules as the third component, J. Mater. Chem. C. 11 (2023) 2921–2929.
[26] X. Ding, Z. Li, The effect of the third component on high performance ternary organic solar cells: a review, J. Polym. Sci. 61 (2023) 3022–3038.
[27] Y. Cai, Y. Li, R. Wang, H. Wu, Z. Chen, J. Zhang, Z. Ma, X. Hao, Y. Zhao, C. Zhang, F. Huang, Y. Sun, A well-mixed phase formed by two compatible non-fullerene acceptors enables ternary organic solar cells with efficiency over 18.6, Adv. Mater. 33 (2021) 2101733.
[28] B. Deng, H. Lian, B. Xue, R. Song, S. Chen, Z. Wang, T. Xu, H. Dong, S. Wang, Niobium-carbide MXene modified hybrid hole transport layer enabling high-performance organic solar cells over 19%, Small 19 (2023) 2207505.
[29] J. Guo, B. Qiu, X. Xia, J. Zhang, S. Qin, X. Li, X. Lu, L. Meng, Z. Zhang, Y. Li, Miscibility regulation and thermal annealing induced hierarchical morphology enables high-efficiency all-small-molecule organic solar cells over 17%, Adv. Energy Mater. 13 (2023) 2300481.
[30] C. He, Y. Pan, Y. Ouyang, Q. Shen, Y. Gao, K. Yan, J. Fang, Y. Chen, C. Ma, J. Min, C. Zhang, L. Zuo, H. Chen, Manipulating the D:A interfacial energetics and intermolecular packing for 19.2% efficiency organic photovoltaics, Energy Environ. Sci. 15 (2022) 2537–2544.
[31] X. Kong, J. Zhang, L. Meng, C. Sun, X. Jiang, J. Zhang, C. Zhu, G. Sun, J. Li, X. Li, Z. Wei, Y. Li, Low-cost and high performance polymer solar cells with efficiency insensitive to active layer thickness, CCS Chem. 5 (2023) 2945–2955.
[32] M. Jiang, H. Zhi, B. Zhang, C. Yang, A. Mahmood, M. Zhang, H. Woo, F. Zhang, J. Wang, Q. An, Controlling morphology and voltage loss with ternary strategy triggers efficient all-small-molecule organic solar cells, ACS Energy Lett. 8 (2023) 1058–1067.
[33] R. Sun, Y. Wu, X. Yang, Y. Gao, Z. Chen, K. Li, J. Qiao, T. Wang, J. Guo, C. Liu, X. Hao, H. Zhu, J. Min, Single-junction organic solar cells with 19.17% efficiency enabled by introducing one asymmetric guest acceptor, Adv. Mater. 34 (2022) 2110147.
[34] C. He, Q. Shen, B. Wu, Y. Gao, S. Li, J. Min, W. Ma, L. Zuo, H. Chen, Simultaneous improvements in efficiency and stability of organic solar cells via a symmetric-asymmetric dual-acceptor strategy, Adv. Energy Mater. 13 (2023) 2204154.
[35] C. Xiao, X. Wang, T. Zhong, R. Zhou, X. Zheng, Y. Liu, T. Hu, Y. Luo, F. Sun, B. Xiao, Z. Liu, C. Yang, R. Yang, Hybrid cycloalkyl-alkyl chain-based symmetric/asymmetric acceptors with optimized crystal packing and interfacial exciton properties for efficient organic solar cells, Adv. Sci. 10 (2023) 2206580.
[36] W. Feng, K. Ma, G. Song, T. Shao, H. Liang, S. Lu, Y. Chen, G. Long, C. Li, X. Wan, Z. Yao, B. Kan, Y. Chen, P-doped all-small-molecule organic solar cells with power conversion efficiency of 17.73, Sci. China Chem. 66 (2023) 2371–2379.
[37] J. Zhang, Z. Ding, B. Kan, B. Lin, X. Wan, W. Ma, Y. Chen, X. Long, C. Dou, J. Zhang, J. Liu, L. Wang, Efficient and thermally stable organic solar cells based on small molecule donor and polymer acceptor, Nat. Commun. 10 (2019) 3271.
[38] B. Kan, Q. Zhang, M. Li, X. Wan, W. Ni, G. Long, Y. Wang, X. Yang, H. Feng, Y. Chen, Solution-processed organic solar cells based on dialkylthiol substituted benzodithiophene unit with efficiency near 10, J. Am. Chem. Soc. 136 (2014) 15529–15532.
[39] J. Zhou, Y. Zuo, X. Wan, G. Long, Q. Zhang, W. Ni, Y. Liu, Z. Li, G. He, C. Li, B. Kan, M. Li, Y. Chen, Solution-processed and high-performance organic solar cells using small molecules with a benzodithiophene unit, J. Am. Chem. Soc. 135 (2013) 8484–8487.
[40] J. Yin, W. Zhou, Q. Ai, X. Meng, S. Liu, Z. Yu, J. Zeng, Y. Chen, DR3TBDTT based ternary blends containing conjugated polymers: crystallization determines morphology and performance, Chin. J. Chem. 36 (2018) 437–442.
[41] K. Ma, Y. Feng, H. Liang, H. Chen, Y. Wang, X. Wan, Z. Yao, C. Li, B. Kan, Y. Chen, Modulation of alkyl chain length on the thiazole side group enables over 17% efficiency in all-small-molecule organic solar cells, Adv. Funct. Mater. 33 (2023) 2214926.

[42] J. Li, C. Zhang, X. Zhong, W. Deng, H. Hu, K. Wang, End-group engineering of chlorine-trialkylsiylthienyl chain-substituted small-molecule donors for high−efficiency ternary solar cells, Small 19 (2023) 2205572.
[43] C. Zhang, J. Li, W. Deng, J. Dai, J. Yu, G. Lu, H. Hu, K. Wang, 18.9% efficiency ternary organic solar cells enabled by isomerization engineering of chlorine-substitution on small molecule donors, Adv. Funct. Mater. 33 (2023) 2301108.
[44] D. Hu, Q. Yang, H. Chen, F. Wobben, V. Singh, T. Liu, R. Ma, H. Tang, L. Koster, T. Duan, H. Yan, Z. Kan, Z. Xiao, S. Lu, 15.34% efficiency all-small-molecule organic solar cells with an improved fill factor enabled by a fullerene additive, Energy Environ. Sci. 13 (2020) 2134–2141.
[45] J. Yao, B. Qiu, Z. Zhang, L. Xue, R. Wang, C. Zhang, S. Chen, Q. Zhou, C. Sun, C. Yang, M. Xiao, L. Meng, Y. Li, Cathode engineering with perylene-diimide interlayer enabling over 17% efficiency single-junction organic solar cells, Nat. Commun. 11 (2020) 2726.
[46] Y. Qin, S. Zhang, Y. Xu, L. Ye, Y. Wu, J. Kong, B. Xu, H. Yao, H. Ade, J. Hou, Reduced nonradiative energy loss caused by aggregation of nonfullerene acceptor in organic solar cells, Adv. Energy Mater. 9 (2019) 1901823.
[47] D. Li, L. Zhu, X. Liu, W. Xiao, J. Yang, R. Ma, L. Ding, F. Liu, C. Duan, M. Fahlman, Q. Bao, Enhanced and balanced charge transport boosting ternary solar cells over 17% efficiency, Adv. Mater. 32 (2020) 2002344.
[48] S. Chen, L. Hong, M. Dong, W. Deng, L. Shao, Y. Bai, K. Zhang, C. Liu, H. Wu, F. Huang, A polyfluoroalkyl-containing non-fullerene acceptor enables self-stratification in organic solar cells, Angew. Chem. Int Ed. Engl. 62 (2023) 202213869.
[49] C. Zhao, J. Wang, X. Zhao, Z. Du, R. Yang, J. Tang, Recent advances, challenges and prospects in ternary organic solar cells, Nanoscale 13 (2021) 2181–2208.
[50] Q. An, F. Zhang, J. Zhang, W. Tang, Z. Deng, B. Hu, Versatile ternary organic solar cells: a critical review, Energy Environ. Sci. 9 (2016) 281–322.
[51] Y. Yan, Y. Zhang, Y. Liu, Y. Shi, D. Qiu, D. Deng, J. Zhang, B. Wang, M.A. Adil, K. Amin, W.A. Memon, M. Wang, H. Zhou, X. Zhang, Z. Wei, Simultaneously decreasing the bandgap and *Voc* loss in efficient ternary organic solar cells, Adv. Energy Mater. 12 (2022) 2200129.
[52] B. Kan, Q. Zhang, F. Liu, X. Wan, Y. Wang, W. Ni, X. Yang, M. Zhang, H. Zhang, T. P. Russell, Y. Chen, Small molecules based on alkyl/alkylthio-thieno[3,2-b] thiophene-substituted benzo[1,2-b:4,5-b′]dithiophene for solution-processed solar cells with high performance, Chem. Mater. 27 (2015) 8414–8423.
[53] J. Kim, C. Song, B. Kim, I. Kang, W. Shin, D. Hwang, Thieno[3,2-b]thiophene-substituted benzo[1,2-b:4,5-b′]dithiophene as a promising building block for low bandgap semiconducting polymers for high-performance single and tandem organic photovoltaic cells, Chem. Mater. 26 (2014) 1234–1242.
[54] Y. Li, C. Chang, Y. Chen, Y. Song, C. Li, H. Yip, A. Jen, C. Li, The effect of thieno [3,2-b]thiophene on the absorption, charge mobility and photovoltaic performance of diketopyrrolopyrrole-based low bandgap conjugated polymers, J. Mater. Chem. C. 1 (2013) 7526–7533.
[55] J. Pommerehne, H. Vestweber, W. Guss, R.F. Mahrt, H. Bässler, M. Porsch, J. Daub, Efficient two layer leds on a polymer blend basis, Adv. Mater. 7 (1995) 551–554.
[56] H. Fan, H. Yang, Y. Wu, O. Yildiz, X. Zhu, T. Marszalek, P.W.M. Blom, C. Cui, Y. Li, Anthracene-assisted morphology optimization in photoactive layer for high efficiency polymer solar cells, Adv. Funct. Mater. 31 (2021) 2103944.
[57] F. Wu, Y. Hsiao, F. Chien, P. Chen, C. Kuo, M. Huang, C. Hsu, Surface plasmonic effects of metallic nanoparticles on the performance of polymer bulk heterojunction solar cells, ACS Nano 5 (2011) 959–967.
[58] M. Lenes, M. Morana, C. Brabec, P.W.M. Blom, Recombination-limited photocurrents in low bandgap polymer/fullerene solar cells, Adv. Funct. Mater. 19 (2009) 1106–1111.
[59] L. Koster, V.D. Mihailetchi, R. Ramaker, P.W.M. Blom, Light intensity dependence of open-circuit voltage of polymer:fullerene solar cells, Appl. Phys. Lett. 86 (2005) 123509.
[60] D. He, M. Zeng, Z. Zhang, Y. Bai, G. Xing, H. Cheng, Y. Lin, Exciton diffusion and dissociation in organic and quantum-dot solar cells, SmartMat 4 (2023) 1176.
[61] K. Sun, Z. Xiao, S. Lu, W. Zajaczkowski, W. Pisula, E. Hanssen, J.M. White, R. M. Williamson, J. Subbiah, J. Ouyang, A.B. Holmes, W.W. Wong, D.J. Jones, A molecular nematic liquid crystalline material for high-performance organic photovoltaics, Nat. Commun. 6 (2015) 6013.
[62] A.B. Svante Nilsson, Andrzej Budkowski, Ellen Moons, Morphology and phase segregation of spin-casted films of polyfluorene/PCBM blends, Macromolecules 40 (2007) 8291–8301.
[63] S. Zeiske, O.J. Sandberg, N. Zarrabi, W. Li, P. Meredith, A. Armin, Direct observation of trap-assisted recombination in organic photovoltaic devices, Nat. Commun. 12 (2021) 3603.
[64] S. Liu, J. Yuan, W. Deng, M. Luo, Y. Xie, Q. Liang, Y. Zou, Z. He, H. Wu, Y. Cao, High-efficiency organic solar cells with low non-radiative recombination loss and low energetic disorder, Nat. Photonics 14 (2020) 300–305.
[65] U. Rau, B. Blank, T.C.M. Müller, T. Kirchartz, Efficiency potential of photovoltaic paterials and devices unveiled by detailed-balance analysis, Phys. Rev. Appl. 7 (2017) 044016.
[66] K.D. Rosenthal, M.P. Hughes, B.R. Luginbuhl, N.A. Ran, A. Karki, S.J. Ko, H. Hu, M. Wang, H. Ade, T.Q. Nguyen, Quantifying and understanding voltage losses due to nonradiative recombination in bulk heterojunction organic solar cells with low energetic offsets, Adv. Energy Mater. 9 (2019) 1901077.
[67] L. Zhang, D. Deng, K. Lu, Z. Wei, Optimization of charge management and energy loss in all-small-molecule organic solar cells, Adv. Mater. (2023) 2302915.

Jing Li received her M.S. degree from the Central South University, Changsha in 2021. She is presently a Ph. D. candidate at Northwestern Polytechnical University (NPU). Her research interests focus on organic photovoltaic materials and organic solar cells.

Chenyang Zhang is a joint doctoral candidate of Hoffmann Institute of Advanced Materials (China) and Northwestern Polytechnical University (China), majoring in flexible electronics. In 2023, he received his M.Eng. degree in materials science under the supervision of Associate Prof. Hanlin Hu and Prof. Kai Wang. At present, his research interests include material design, synthesis, device preparation, and characterization of organic solar cells.

Xiaokang Sun received his Master's degree from Xiangtan University in 2022. He is currently a joint Ph.D. student of the Xiangtan University and the Hoffmann Institute of Advanced Materials. His research interests mainly focus on the device engineering for organic solar cells and the application of the small angle X-ray scattering technique on photovoltaic materials.

Hanlin Hu obtained his Ph.D. degree in the Department of Materials Science and Engineering at King Abdullah University of Science & Technology in Saudi Arabia in 2017. He carried out his postdoctorate research in Prof. Gang Li's group at the Hong Kong Polytechnic University. He is currently an associate professor at Hoffmann Institute of Advanced Materials, Shenzhen Polytechnic University. He has built the Synchrotron and Printable Electronic Devices Lab at HIAM equipped with in-house GIWAXS/GISAXS. He has published 120+ articles with an H-index of 31. His research focuses on printing thin film solar cells and transistors, and the synchrotron-based phase-transition study.

Kai Wang received his B.S. (2009) and Ph.D. degrees (2014) under the supervision of Prof. Yue Wang in the Jilin University (China). Then, he worked at the King Abdullah University of Science & Technology as a Postdoctoral Researcher with Prof. Stefaan De Wolf. In 2020, he obtained his current professor position in the Northwestern Polytechnical University (China) to continue his research interest including design and synthesis of novel organic optoelectronic functional materials and their photovoltaic devices fabrication.